Volume 10, Issue 3, 2020, 5361 - 5368 ISSN 2069-5837
Biointerface Research in Applied Chemistry
www.BiointerfaceResearch.com
https://doi.org/10.33263/BRIAC103.361368
Original Research Article Open Access Journal
Received: 10.02.2020 / Revised: 04.03.2020 / Accepted: 05.03.2020 / Published on-line: 09.03.2020

Simulation of droplet ejection based on electromechanical parameters & chemical condition for controlling inkjet printing devices

Dung My Thi Dang [1,2], Majid Monajjemi [1, 3, *], Fatemeh Mollaamin [1], Chien Mau Dang [1,2, *]

[1]Institute for Nanotechnology (INT) Community 6, Linh Trung Ward, Thu Duc District, Ho Chi Minh City, 700000, Vietnam
[2]Vietnam National University Ho Chi Minh City, Community 6, Linh Trung Ward, Thu Duc District, Ho Chi Minh City, 700000, Vietnam
[3]Department of Chemical Engineering, Central Tehran Branch, Islamic Azad University, Tehran, Iran
*corresponding author e-mail address: ***dmchien@yahoo.com; maj.monajjemi@iauctb.ac.ir*** | Scopus ID 54406655100; 6701810683

ABSTRACT

In this study, the droplets in inkjet printing have been simulated based on mechanical parameters including temperature and pressure changing and also the chemical condition contain dielectric of various solvent materials has been investigated. Basically in viewpoint of electromechanical parameters we simulated and divided the inkjet printing into the piezoelectric type and thermal type, and as our results shows, each type has advantages and disadvantages. In this paper the piezoelectric types which has features such as; ink delivery quantity, driving control, controlling of droplet size based on color representation, generating heat and superb reliability have been introduced. By this work, we exhibit the deformation of piezoelectric elements is applied in two ways, consist of thickness deformation and sliding deformation. This chamber is included in a small slot that is created through two piezoelectric crystal plates .In addition the voltages inserted to the piezoelectric walls on both sides cause deformation mode. Due to this operation shear mode deformation occurs to both walls and via the ink pressure chamber, ink drops are delivered. Several inks applied as a dielectric material layers for conductive track in electrochemical sensors. Thus, passivation of printed sensors and deposition of adhesives can be achieved simultaneously. In this work, the presented method for the printing of UV-curable adhesive and dielectric inks demonstrates a rapid facile prototyping process.

Keywords: *piezoelectric constant; Droplet Ejection; Inkjet Printing Devices; dielectric inks.*

1. INTRODUCTION

The growth of a manufacturing system is related to the needs of automation, miniaturization, reductions in costs and considerations of environmental factors. Therefore, inkjet printing technologies are becoming a suitable alternative for patterning of materials in a range variety of applications. /Inkjet printing systems also have numerous potential in the applications of flat panel displays such as Organic light emitting diode (OLED) which is one of the important technologies for future. Unfortunately, due to the restriction in the option of solvents, OLED is generally fabricated via the thin film depositions (evaporation process and patterning through lithography). These technologies are very difficult and expensive, therefore massive benefits might be provided if a compositions of organic light emitting materials combined directly by inkjet printing methods[1]. The current methods for polymers light emitting diodes (PLED) are applied mostly in the fabrication of single color, but via using inkjet printing technologies, it is possible to produce variant and tiny pixels such as red, green and blue units for fabricating the colorful filters. Comparing with the coating methods, inkjet printing systems have the advantages of high resolution, capability for the production of large panels with low cost and environmental friendliness [2]. Several varieties of actuation methods have been accomplished for ejecting liquid droplets, including piezoelectric, acoustic, thermal bubble, electro-static [3]. Among these techniques, piezoelectric thermal bubbles methods are most mature and common for the commercial inkjet printers. The ejection of droplets through the nozzle are induced either via the displacement of a piezoelectric diaphragm (which includes the fluid) or through the formation of a vapor bubble in the ink via the heating of a resistive film (Scheme 1).

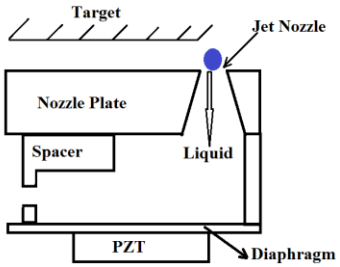

Scheme 1. A schematic diagram of a piezoelectric inkjet print head.

For piezoelectric inkjet printing, there is not necessary to vaporize the fluid. Therefore, it can be applied in ejection and dispensing of polymer and also liquid metals. In viewpoint of printing quality, the piezoelectric inkjet printing technologies in the electronic industry are very much favorable due to that of the ejected droplet. Thus, it is needed to investigate the novel knowledge of the mechanism of forming liquid droplet, ejected condition and impact on the substrate in a piezoelectric inkjet printing device. With the knowledge of these phenomena, it is then possible to control the sizes of droplet, improve consistencies of droplet, and eliminate bubble droplet through right designing of the instruments based on physical properties of liquids. Basically, the mechanism of the inkjet printing can be divided into two sections. One is to understanding how droplet is formed and the other understands how much the droplets can be fixed onto the substrate. Droplet formation in inkjet printing can be investigated via numerical simulations that had been employed by a number of researchers. Bogy and Shine [4], exhibited a model for calculating the transient solution for the figure changing and velocities in a semi-infinite liquid column, under the effects of periodic micro-

perturbation at the nozzle. In other works by Fromm and Res, figure evolution of ejected droplets has been simulated with the actuation through a driving pressure, which is a square wave function of time, at the outlet of the nozzle [5]. The stream position can be presented through the Navier-Stokes equations in an axial symmetrical orientation via solving a finite-difference algorithm in the Lagrangian computational mesh. Previously Asia in 1992, investigated a three-dimensional finite difference pattern based on the VOF method for solving Navier-Stokes equation and predicted the situation of drop ejection in the bubble jet printer [6]. Liou and coworkers used a fluid dynamics simulation devise; named COMET, for predicting the meniscus position with time inside a SEA-Jet inkjet print-head during all steps of the infusion and ejection stages [7]. Although many studies were accomplished for simulating the formation of the droplets through either bubbling or electrostatic approach, there a few studies on the simulation of a droplet shape with the actuation of piezoelectric-push mode. Fukai and coworkers exhibited the wet-abilities of the layers upon which the droplet impinges were found to affect considerably all phases of the spreading process and the spreading radiuses straightly corresponded to the droplet impact velocities. The contact angles, which were determined experimentally, were used as inputs to the numerical model [8]. Hatta et al [9]. understood that the deformation action of a droplet on the solid surfaces cannot not only be specified using only the Weber and Reynolds Numbers but also other parameters such as initial kinetics of the droplet and the conditions of the substrate have to be considered. Pasandideh & Qiao applied both experimental and numerical methods for modeling droplet deformation based on the influence of surface tension and impact dynamics of a water droplet during falling on the surface stainless steel [10]. The results exhibited that as surface tension of the droplet decreased, the spreading radius became smaller and recoil height became shorter. Obviously, the issue of initial velocities of the droplet needs to be taken into consideration, which is one of the key issues treated in inkjet printing, including the formation, ejection, and impact of liquid droplet on the substrate.

2. MATERIALS AND METHODS

2.1. Background of simulation.

2.1.1. Operation points.

The deformation of piezoelectric elements is applied in two ways, consist of thickness deformation and sliding deformation. This chamber is included in a small slot that is created through two piezoelectric crystal plates. In addition the voltages inserted to the piezoelectric walls on both sides cause deformation mode. Due to this operation shear mode deformation occurs to both walls and via the ink pressure chamber, ink drops are delivered. In this paper the piezoelectric types which has features such as; ink delivery quantity, driving control, controlling of droplet size based on color representation, generating heat and superb reliability have been introduced. By this work, we exhibit the deformation of piezoelectric elements is applied in two ways, consist of thickness deformation and sliding deformation (scheme 2-a).

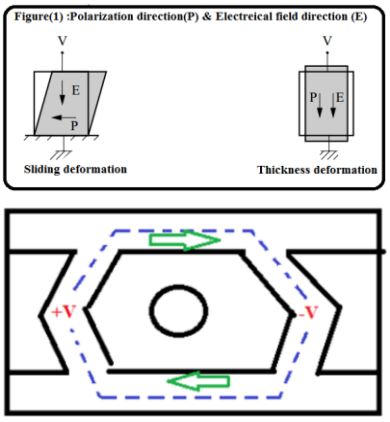

Scheme 2. exhibits an operation rule of an ink pressure chamber.

The latter utilizes sliding deformation, which is generated by applying an electric field perpendicular to the polarization direction of the piezoelectric element. Scheme2 –b, exhibits the operation principle of an ink pressure chamber under voltage changing(ΔV). This chamber is included in a small slot that is created through two piezoelectric crystal plates. In addition the voltages inserted to the piezoelectric walls on both sides cause deformation mode. Due to this operation shear mode deformation occurs to both walls and via the ink pressure chamber, ink drops are delivered.

2.1.2. Dielectric materials.

Several inks applied as a dielectric material layers for conductive track in electrochemical sensors. Thus, passivation of printed sensors and deposition of adhesives can be achieved simultaneously. In this work, the presented method for printing of UV-curable adhesive and dielectric inks demonstrates a rapid facile prototyping process. For our simulation by this work we focused on the printing of high-dielectric constant of various material layers, which are among the essential building blocks for electronic components such as thin-film capacitors and field-effect transistors for transparent electronics. For instance, tantalum (V) oxides have high dielectric constant, a high refractive index, and also high chemical stabilities [11]. The homogeneity of the electric fields across the dielectric layers is crucial for the proper operation, therefore any variations in the thickness uniformity would result in a deterioration of the efficiency. Our simulation indicates that besides the design of the solvent mixture and dielectric constant (ε_r), related to the viscosity and surface-tension criteria the volatility of the solvents in the ink completely influence the thickness uniformity of the deposit and consequently the efficiency of the printed.

2.1.3. Navier-Stokes Equation.

Navier–Stokes equations [12] are useful because they explain the non-classical physics of many phenomena of scientific and engineering research. They can be used to model and analyses the statically data of a weak flow in a pipe or drop ejection in a bubble jet printer. The solution of λ the Navier–Stokes equations is based on flow velocity. Once the velocity situation is calculated other physical data, such as pressure or temperature, can be found through additional related equations. Studying velocity instead of position (which is used in classical mechanics) makes more sense for a fluid [13].

The Navier–Stokes momentum equation can be derived as a particular form of the Cauchy momentum equation, whose general convective form is $\rho \frac{Du}{Dt} = -\nabla P + \nabla . \tau + \rho g$ **(1)** where, $\frac{D}{Dt}$

is mathematical derivative, ρ is density, P is pressure, u is the flow velocity, "t" is time and τ is the stress tensor with order two this equation of momentum is important for simulating the dye-based inks which are used in some inkjet printing for diluting the polymer solution in water. This equation can be rewritten in view point of a comprisable flow or compressible momentum Navier–Stokes equation through Cauchy stress tensor as: $\sigma = \lambda(\nabla . u)I + 2\mu\varepsilon$ **(2)**, which "I" is the identity tensor and $\nabla . u$ is the rate of expansion flow and the trace of the stress tensor in three dimensions is shown as: Trace (σ)= $(3\,\lambda + 2\mu)\,\mu$**(3).** From the equations 2&3 second viscosity can be defined as: $\zeta \equiv \lambda + \frac{2}{3}\mu$ **(4).** Both dynamic viscosity (μ) and second viscosity (ζ) must be constant; usually, both dynamic and second viscosities are related to the density. Although the viscosity is expressed through pressure, incompressible flows it would be interpreted by temperature [14]. Since the divergence of $\nabla\mathbf{u}$ & $(\nabla\mathbf{u})^{\mathrm{T}}$ tensors are$\nabla^2\mathbf{u}$ & $[\nabla(\nabla\cdot\mathbf{u})$ (known as Lamb Vector)] respectively, the most general Navier–Stokes momentum equation can be written as: $\rho\frac{Du}{Dt} = -\nabla\bar{P} + \mu\nabla^2\mathrm{u} + \frac{1}{3}\mu\nabla(\nabla . u) + \rho g$ **(5).** It is notable the volume viscosity "ζ" is a mechanical pressure and is not equal to a thermodynamic pressure which can be defined as $\bar{P} \equiv P - \zeta\nabla\mathrm{u}$ **(6).** To formulate the incompressible momentum Navier–Stokes equation it might be considered the Stokes' stress constitutive equation as $\tau = 2\mu\varepsilon$ where the rate-of-strain tensor is: $\varepsilon = 1/2(\nabla\mathbf{u} + (\nabla\mathbf{u})^{\mathrm{T}})$ then the Stokes's stress constitutive equation which only used for incompressible viscous fluids is yielded as $\tau = \mu(\nabla\mathrm{u} + (\nabla\mathrm{u})^{\mathrm{T}})$ **(7).** Here the Dynamic viscosity μ might not be constant due to depending on density and also on pressure. Due to zero value for $\nabla\mathrm{u} = 0$ in an in-compressible fluid, the incompressible momentum Navier–Stokes equation can be rewritten as: $\frac{\partial u}{\partial t} + (\mathbf{u}.\nabla)\mathbf{u} - \vartheta\nabla^2\mathrm{u} = -\nabla\omega + \mathbf{g}.$ **(8)** which $\vartheta = \mu/\rho_0$ is kinematic viscosity [20]. There are five parts in the equation 8 (from left two rights) which indicate in terms of variation $(\frac{\partial u}{\partial t})$, conviction $((\mathbf{u}.\nabla)\mathbf{u})$, diffusion $(\vartheta\nabla^2\mathrm{u})$, internal source $(= -\nabla\omega)$ and external source $(\mathbf{g}.)$ respectively. The vector Laplacian "$\mu\nabla^2\mathbf{u}$**"** is the difference between the velocity at a point and the mean velocity in a small surrounding volume (it is an important physical parameter for inkjet printing) while this parameter implies the *diffusion of momentum*. So the incompressible Navier–Stokes equation leads to a vector diffusion which is named "Stokes equations", therefore incompressible Navier–Stokes equations are related to the series equation of convection-diffusion [15, 16]. Vector operators are defined in terms of Del, including the gradient (∇), divergence (∇.), and Curl (∇ ×). Using the curl of the Navier–Stokes equation yields a term in the removing of pressure. By assuming $u_z = 0$ the equation can be written as: $\rho(\frac{\partial u_x}{\partial t} + u_x\frac{\partial u_x}{\partial x} + u_y\frac{\partial u_x}{\partial y}) = -\frac{\partial p}{\partial x} + \mu\left(\frac{\partial^2 u_x}{\partial x^2} + \frac{\partial^2 u_x}{\partial y^2}\right) + \rho g_x$ **(9)**

$\rho(\frac{\partial u_y}{\partial t} + u_x\frac{\partial u_y}{\partial x} + u_y\frac{\partial u_y}{\partial y}) = -\frac{\partial p}{\partial y} + \mu\left(\frac{\partial^2 u_y}{\partial x^2} + \frac{\partial^2 u_y}{\partial y^2}\right) + \rho g_y$ **(10).**

The equations 9&10 describe the two dimensional of stream functions, where density unit (ρ) is kgM^{-3} and viscosity (μ) is Pascal second, meanwhile the unit of velocity "u" and Pressure (p) are m.s^{-1} and Pascal respectively. In addition g_y and g_x are the acceleration components due to gravity in y- and x-directions. With defining a new parameter as stream function "Ψ" which is a definition for Incompressible flows in two dimensions as :$\{u_x = \frac{\partial\Psi}{\partial y}\frac{\partial\Psi}{\partial y}, u_y = \frac{\partial\Psi}{\partial x}\}$ and the conservation of mass for incompressible flow is:$\frac{\partial\Psi}{\partial y} + \frac{\partial\Psi}{\partial x} = 0$ **(11)**

2.2. Methodology for simulation.

As mentioned the generation of inkjet droplets is a function of several variables therefore various knowledge such as physics and fluid mechanics are needed. For understanding the jetting phenomena of the liquid droplets the concept of pressure waveform, numerical analysis are necessary. For most applications, it is very important that only a single drop is generated. However, occasionally, extra drops are also generated. These drops are called satellite drops.

These satellites can easily lose properties and destroyed printing quality which this phenomenon of satellites that result from the liquid thread breakup (LTB) and is well known as the Rayleigh instability. The drop formation of the liquids thread is needed to be considered in the drip and continuous condition, especially in viscous liquids [17-21]. Although for drop-on-demand inkjet process, the LTBs are along with the perturbation of the acoustic waves, thus the linear analysis of Rayleigh does not predict the formation of satellites at all. In addition, the subsequent theories have predicted satellites but do not explain their detailed behavior. Fromm and coworkers [22] identified the Ohnesorge number (Oh) which is regarded as the suitable grouping of physical parameter constants to describe drop formation. By this definition the parameter $Z = \frac{1}{Oh}$ and proposed that $Z > 2$ for stable drop generation. This analysis was further refined by Reis &Derby [23], who applied numerical simulation of drop growth to indicate the following range, $1 < Z < 10$, for position of a droplet growth. At the low amount of Z, viscous situation prevents drop ejection, while at high amounts the primary drops are included with a large number of satellite droplets. $Z = \frac{(\alpha\gamma\rho)^{\frac{1}{2}}}{\eta}$ **(12)** which v, γ, ρ and η are the average velocity, densities, surfaces tensions, and viscosities, respectively. And α is also a characteristic dimension related to the diameter of the printing nozzle. A restricted condition for drops is the influence of fluid/air surface tension at the nozzle which must have enough energy for overcoming these barriers for an ejection. Duineveld and coworkers [24] calculated a minimum velocity V_{min} for drop ejection based on equation as follows $V_{min} = (\frac{4\gamma}{\rho d_n})^{0.5}$ **(13)** which d_n is the nozzle diameter. The behavior and efficiency of an inkjet printing process are strongly related to the coupling of elasticity, piezoelectricity, and free surfaces (from fluid dynamics). The pressure can be estimated through propagation theory of an acoustic wave at the nozzle [25, 26] which can be considered as a sine wave. The bubbles can be growing when the acoustic pressure variations are strong enough. By a Maximum pressure air is squeezed out of the bubble, but this loss is overcompensated at the pressure minima when the bubble expands. The net gas diffusion into the bubble is a result of a surface effect and a shell effect, e.g. an expanded bubble can absorb more air because of its wide surface area and the higher concentration gradient of the dissolved air in the liquid around the bubble, which is compressed by the expanding bubble.

2.2.1. Drop-on-demand (DOD) in electromechanical properties.

Although ink jet printing is applied for depositing Pico liter drops on various targets, the fundamental dynamics of DOD ink jet drop formation and impaction on substrates are not yet well understood. This is mainly due to the key stages during drop formation and impaction last less than 100 s for a micron scale. The main obstacle of DOD ink jet printing is the "first drop problem" (FDP) which related to the first few drops ejected through a nozzle [27]. The FDP is due to the evaporation of ink at the nozzle exit and the quantity of evaporation related to the vain and void time of the nozzle. It is notable that FDP in many ink jet printing applications including liquids such as macromolecules, colloids and other complex fluids, is serious due to the concentration of the suspended materials. The investigation of the behavior of those liquids in DOD drop formation and impaction is challenging. Parameters of DOD drop formation for the four driving signals described in Table 1.

Table 1. Parameters of four driving signals extracted of Ref.28 [28].

Signal	Voltage volts	Rising time $T1$ (μs)	Falling time $T2$ (μs)	Dead time $T3$ (μs)	Rising time $T4$ of small pulses (μs)	Falling time $T5$ of small pulse (μs)
1	21.6	10.6	2.6	5.3	4.4	3.0
2*	21.6	10.6	2.6	-	-	-
3	21.6	14.4	2.6	5.3	4.4	3.0
4	21.6	10.6	5.0	2.4	4.4	3.0

*Single-peak wave form.

When a pressure wave moves inside the liquid through the nozzle, liquid is throw out and then the velocity difference between the column head and the liquid exit causes the liquid column to stretch. During the stretching of the liquid column, the liquid at the tail exit from the nozzle. Draw back of the liquid occurs because the pressure is high in the tip of the tail at pinch off due to the small radius of curvature. During the shrinkage of the liquid thread, a second neck near the bulbous head appears. The radius of the neck may continuously decrease until the liquid thread breaks up into two parts and therefore the secondary liquid thread contracts into a satellite.

Consequently, based on its velocity and its size (primary drop and satellite), recombination of the primary drop and satellite can occur. If the satellite does not merge with the primary drop, the accuracy of material deposition on substrates is spoiled. Deletion of satellites is necessary for DOD ink jet printing, especially in the delivery of the functional material. Although the voltage amplitudes of the four driving signals are the same (Table 1), wave form differences lead to four distinct drop formation processes. This is due to the smaller pulse producing negative pressure suction within the nozzle, which promotes the stretching and necking of the liquid thread. In addition, under the action of the smaller pulse, the pinch off of liquid from the nozzle exit is more uniform, with less influence from the nozzle plate. The kinetic energies and volume of the ejected liquids produce through the initial larger pulses. Hence, the double-peak wave form produces a smaller primary drop and satellite with a lower speed (Table 2).

Table 2. Effect of four wave forms on DOD drop formation extracted of Ref.28 [28]

Signal	Time of pinch off nozzle (μs)	Length of liquid thread (μm)	Velocity of primary or final drop (m/s)	Diameter of primary drop (μm)	Diameter of satellites ±1 (μm)
1	28	148.3	3.4	43.0	27.5
2	42	231.5	4.1	45.1	33.0
3	30	210.3	5.0	45.6	36.6
4	28	171.0	4.0	44.9	31.8

Based on data in table 1, both of the signals are double-peak wave forms, but the rising time, T1, is 10.6 s for signal 1 and is 14.4 s for signal 3, meanwhile increasing of T1 causes the liquid thread length is change(from 148.3 to 210.3 μm in Table 2). And also the primary drop and satellite become bigger. Consequently the velocity of the primary drop corresponds to the time over which the Piezo transducer contracts causing the ink chamber to develop that draw in ink. If T1 is too small, the system has not sufficient time to respond and insufficient ink is sucked into the chamber. On the other hand, if T1 is too large, air may be sucked into the nozzle and cause jet ability problems. Therefore, an appropriate rising time, which depends on not only the geometry and material of print-head, but also the liquid properties such as viscosity, is required.

Quantitative analysis of DOD drop formation is essential in understanding how the inkjet parameters affect drop formation.

2.2.2. Chemical condition & polymer solutions in drop-on-demand.

Recently, inkjet printing has developed and applied as a crucial technology for both graphical printing and digital fabrication through well-defined spatial deposition of solutions. The dynamics of drop formation have been widely studied numerically using both one and two-dimensional approaches. Computational analysis of the drop-on-demand inkjet process has been also developed in wide range [29]. Although in DOD printing individual ink drops suddenly are ejected via a nozzle in response to an impulse, understanding their mechanism through this methods is obligatory for any further development of inkjet technologies. Obviously, the sizes of the droplets ejected are equivalent to the nozzle diameter, however, new novel techniques have been developed to alter droplet radius into the main drop or breakup into small satellite drops [30]. Based on Navier–Stokes (equations 1-12) of fluids, stable drop generation without satellites is limited to a narrow range of viscosities corresponding roughly to the Ohnesorge numbers in the range 0.1–1 , therefore adding the polymer molecules can considerably affect the breakup of liquid filaments produced via flow by a nozzle [31]. On the other words polymer content affects the validity of jetting; print speed may be compromised and, at high concentrations, the main drop may even fail to detach from the nozzle. Three items of jetting behavior are explained through the prevailing mechanism which consists of jet speed (is restricted by zero-shear viscosity), viscoelasticity and high strain rate extensional viscosity. The transitions between these items are determined via the initial "Weissenberg" number $Wi_0 = U_0 \frac{\tau}{D}$, where U_0 , is the jet speed at the nozzle exit, τ is the fluid relaxation time and D is the nozzle diameter. The first transition from item 1 to 2 occurs at $Wi_0 = 0.5$ at which point polymers can become significantly extended from

their equilibrium configuration. The second transition from item 2 to 3 occurs at $Wi_0 = L$, when polymers reach their finite extensibility limit L. The velocity U of a general fluid with density ρ and pressure P is explained via the usual conservation of momentum equation of Navier-Stokes Equation (Equation 1) and the stress tensor $\boldsymbol{\sigma}$ is determined from the equation 2, consequently the total stress based on Chilcott–Rallison closure approximation known as the FENE-CR model can be written from the Navier-Stokes Equation as: $\boldsymbol{\sigma} = 2\mu_s \boldsymbol{E} + Gf(\boldsymbol{A} - \boldsymbol{I})$ **(14)** where μ_s is the solvent viscosity, $\boldsymbol{E}$ is the strain rate tensor and the polymer stress consists of the elastic modulus G, the conformation tensor $\boldsymbol{A}$ and the FENE factor f can be written as

$$: f = \frac{L^2}{L^2+3-tr(\boldsymbol{A})}.$$

The conformation tensor A satisfies the evolution equation $\frac{D\boldsymbol{A}}{DT} = \boldsymbol{K}.\boldsymbol{A} + \boldsymbol{A}.\boldsymbol{K}^T - \frac{f}{\tau}(\boldsymbol{A} - \boldsymbol{I})$ **(15),** where τ is the relaxation time of the polymer and $K_{ij} = \frac{\partial u_i}{\partial X_j}$ is the velocity gradient tensor.

In an elastic modulus G, relaxation time τ and finite extensibility L, can be determined as functions of the molecular weight Mw, weight fraction concentration $\emptyset$ and solvent quality factor m using Zimm theory [32]. The elastic modulus is proportional to concentration and inversely proportional to molecular weight $G = \frac{\emptyset RT}{M_w}$ where R is the universal gas constant and T is the absolute temperature. The finite extensibility L can be determined from the ratio of the equilibrium coil to the fully extended length of the polymer so that $L^2 = 3(\frac{jsin^2(\frac{\theta}{2})M_w}{C_\infty M_\mu})^{2(1-\vartheta)}$ where θ is the carbon-carbon bond angle, j is the number of bonds of a monomer unit with molar mass M_μ and C_∞ is the characteristic ratio[33]. Hence, for a dilute mono-disperse polymer solution, the FENECR model. parameters scale with solvent quality factor ϑ it can be shown $G \sim M_W^{-1}$, $\tau \sim M_W^{3\vartheta}$ and $L \sim M_W^{(1-\vartheta)}$ Thus, by using the Zimm model to determine the molecular weight dependence of the relaxation time it can determine how the maximum jet-able polymer concentration scales with molecular weight during each of the three jetting regimes. These scaling laws are summarized in Table 3.

Table 3. Scalings in terms of different concentrations [34].

Concentration	Item 1	Item 2	Item 3
Wt%	$M_W^{(1-3\vartheta)}$	$M_W^{(1-6\vartheta)}$	$M_W^{(-2\vartheta)}$
C	1	$\frac{1}{wi_0}$	$\frac{1}{L}$

Based on our previous works [37-66] we have simulated our model

3. RESULTS

The inkjet printing is a multi-process including piezoelectricity, elasticity and free surface flow. It is suitable to focus on the process of droplet ejection with a partially tapered nozzle as shown in Fig. 1 is considered as the simulation system. When a high voltage electric signal is used, the PZT device bends and causes high pressure on the ink chamber and squirt the ink droplet out of the nozzle. The moving boundary methods are applied to simulate the displacement of PZT diaphragm by this work.

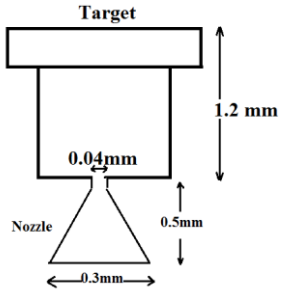

Figure 1. A schematic diagram of the inkjet print head of the modeled system.

The equivalent velocities at the bottom of the nozzle under the voltage pulses are shown in Fig. 2. And consist of four stages in each cycle [35]. In the first step, the velocity rises instantaneously up to 260 cm/s and keeps constant for 16 μs, in the second stage, the velocity falls down directly to zero and keeps for 12 μs. A negative velocity; 260 cm/s, is induced and kept constant for 16 μs in the third stages. Finally, the velocity becomes zero until the end of the cycle. A total period of 220 μs is computed to show the formation of droplet and their impact on the target. The material properties employed in the simulations of various solvents are listed in Table 4.

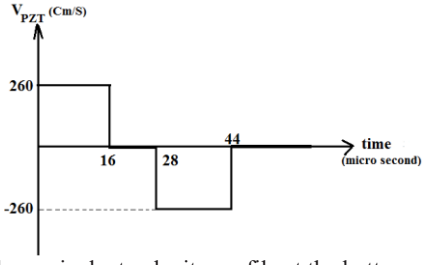

Figure 2. The equivalent velocity profile at the bottom of the nozzle.

Table 4. The necessary parameter of various solvents for simulation.

liquid	Surface tension dyncm^{-1}	Temperature T °C	Density grcm^{-1}	Viscosity cP=mPa.S	Contact angle	Dielectric Constant
water			1.0	1.0		78.54
Isopropanol	21.7	20	0.785	2.86		18.3
***n*-Hexane**	18.4	20	0.659	0.31		1.89
Acetone	23.7	20	0.791	0.32		20.7
***n*-Octane**	21.8	20	0.827	10.6		-
Diethyl ether	17.0	20	0.706	0.24		4.34
Ethanol	22.27	20		1.07	0.0	
polyethylene		20		36		
polystyrene		20		30		
Polyethylene oxide		20		43		

The computed results of the droplet ejection with various surface tensions of liquid at five different situations are exhibited in Fig 2. Although the effect of surface tension is not obvious in these steps, at the second step necking of the ejected liquid occurs at the tip of the nozzle as shown in Fig.2. Since the liquid keeps moving forward, however, the supply of ink liquid from nozzle is stopped. In order to keep a balance between liquid and nozzle, necking appears. At the third step, the droplet with round head and slender tail are formed and the head of the droplet becomes larger as surface tension of the liquid increases. The main droplet separates completely from the nozzle and satellite droplets are

formed at the $50\mu s$, which lies within the F to I steps of the actuation period, as shown in Fig. 3. It can be seen that the droplet with smaller surface tension has a longer tail and moves faster. It can also be seen that a smaller head grows at the tail of the main droplet and it accelerates to catch up with the front head by the action of surface tension.

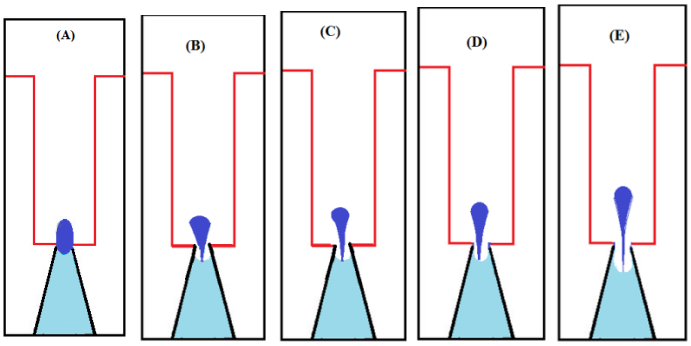

Figure 2. The droplet shapes and velocity profiles with different surface tensions of polymer at 25 μs (surfaces tension are include A=0.02 N/m, B=0.04 N/m, C=0.06 N/m and D=0.08 N/m).

The sloshing of liquid in the nozzle is also found. A liquid with higher surface tension can damp out the sloshing more quickly as shown in Figs. 2&3. It should be noted that the impact velocity of the droplet on the target and the impact time vary with different surface tensions of the liquids. By this work it can be seen that a comprehensive illustration of the inkjet dynamics, that consist of the growth, formation and ejection of the droplets can be referred to the simulations. The effect of tension factors does not appear in the first step when the voltages are applied and the ink liquids are just make force to out the droplets from the nozzle. In the second step, liquids keep moving forward without further product, ink liquid from the nozzle. In the third step, droplet with round head and slender tail are formed. In addition, the head of the droplet grows larger as surface tension of the liquid increases. Based on equations (8-13) data after simulation, a sequence of images during DOD drop formation is shown in Figures 3&4, revealing the main features of this process. The liquid at the nozzle is concentrated to move upward to form meniscus. During the time between T opt and 1.5Topt, the pressure is used and the liquids at the nozzle are accelerated to move downward through the positive pressure. The liquid thread is broken because of the negative pressure between 1.5T opt and 4.5Topt. Breakup of the free liquid thread is going towards the generation of a primary droplets and also satellites. The first satellites drop formation mechanism results from the liquid thread is long. The length and velocity of liquid thread at surface tension and viscosity will direct cause for breakup of the liquid thread. These breakup processes are well known as the Rayleigh instability.

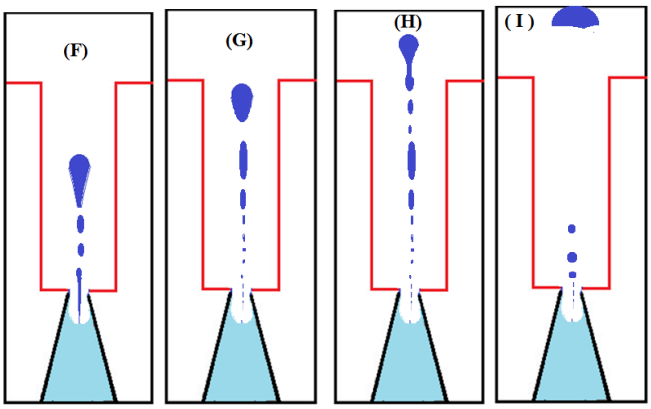

Figure 3. The droplet shapes and velocity profiles with different surface tensions of polymer at 50 μs (surfaces tension are include F=0.10 N/m, G=0.12 N/m, H=0.14 N/m and I=0.16 N/m).

Influence of viscosity on the droplet formation process as described above, the inkjet is a complicated free surface flow of two immiscible fluids of liquid and gas. Viscosity and surface tension of the liquid plays a significant role in the flow behavior. The ejection behaviors of the various liquids of table 4 are simulated under the identical waveform condition. The ejected liquid processes for the various viscosities at different times are simulated too. It can be seen that under identical pressure conditions and surface tension, as the viscosity of the liquid increases, the ejected liquid thread becomes shorter since the resistance of viscosity increases. For viscous liquids, the viscous dissipation will slow down the dynamics of breakup. Therefore, as viscosity of the liquid increases, the speed of droplet becomes slower. As liquid thread becomes longer, the liquid is more unstable and generates more satellites.

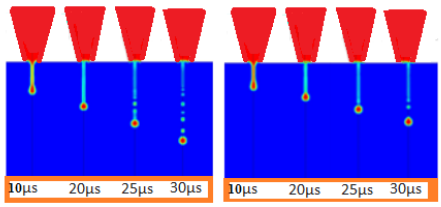

Figure 4. Phases contours of viscosity on the droplet formation.

4. CONCLUSIONS

We exhibit the deformation of piezoelectric elements is applied in two ways, consist of thickness deformation and sliding deformation. This chamber is included in a small slot that is created through two piezoelectric crystal plates. In addition, the voltages inserted to the piezoelectric walls on both sides cause deformation mode.

5. REFERENCES

1. Guillou, O.; Daiguebonne, C.; Calvez, G.; Bernot, K. A long journey in lanthanide chemistry: From fundamental crystallogenesis studies to commercial anticounterfeiting taggants. *Acc. Chem. Res.* **2016**, *49*, 844–856, https://doi.org/10.1021/acs.accounts.6b00058.
2. Wu, H.C.; Lin, H.J. The Japan Institute of Metals, Effect of Actuating Pressure Waveforms on the Droplet Behaviour in a Piezoelectric Inject. *Materials Transactions* **2010**, *51*, 2269–2276, https://dx.doi.org/10.2320/matertrans.M2010123.
3. Rahman, K.K; Ko, J.B.; Khan, S.; Kim, D.S.; Choi, K.H. Simulation of droplet generation through electrostatic forces. *Journal of Mechanical Science and Technology* **2010**, *24*, 307-310, https://doi.org/10.1007/s12206-009-1149-y.
4. Hoth, C.N.; Choulis, S.A.; Schilinsky, P.; Brabec, C.J. High Photovoltaic Performance of Inkjet Printed Polymer:Fullerene Blends. *Adv. Mater.* **2007**, *19*, 3973–3978, https://doi.org/10.1002/adma.200700911.
5. Liu, Q.; Omre, M. High precision solder printing technology and the state-of-the-art. *J. Mater. Proc. Tech.* **2001**, *115*, 271–283, https://doi.org/10.1016/S0924-0136(01)00740-3.

6. Crowley, K.; O'Malley, E.; Morrin, A.; Smyth, M.R.; Killard, A.J. An aqueous ammonia sensor based on an inkjet-printed polyaniline nanoparticle-modified electrode. *Analyst* **2008**, *133*, 391–399, https://doi.org/10.1039/b716154a.
7. Koo, H.S.; Chen, M.; Pan, P.C. LCD-based color filter films fabricated by a pigment-based colorant photo resist inks and printing technology. *Thin Solid Films* **2006**, *515*,896–901, https://doi.org/10.1016/j.tsf.2006.07.159.
8. Tsai, M.H.; Hwang, W.S.; Chou, H.H.; Hsieh, P.H. Effects of pulse voltage on inkjet printing of a silver nano powder suspension. *Nanotechnology* **2008**, *19*, 304.
9. Singh, M.; Haverinen, H.M.; Dhagat, P.; Jabbour, G.E. Inkjet printing- Process and its application. *Adv. Mater* **2010**, *22*, 673–685, https://doi.org/10.1002/adma.200901141.
10. Le, H.P. Progress and Trends in Ink-jet Printing Technology. *Journal of imaging science and technology* **1998**, *42*, 49-62.
11. Hebner, T.R.; Wu, C.C.; Marcy, D.; Lu, M.H.; Strum, J.C. Ink-jet printing of doped polymers for organic light emitting devices. *Appl. Phys. Lett* **1998**, *72*, 519–521, https://doi.org/10.1063/1.120807.
12. Yamaguchi, K.; Sakai, K.; Yamanaka, T.; Hirayama, T. Generation of three-dimensional micro structure using metal jet. *Precision Eng* **2000**, *24*, 2–8, https://doi.org/10.1016/S0141-6359(99)00015-X.
13. Bogy, D.B.; Shine, S.J.; Talke, F.E. Finite difference solution of the Cosserat fluid jet equations. *J. Comput. Phys*. **1980**, *38*, 294–326, https://doi.org/10.1016/0021-9991(80)90151-5.
14. Fromm, J.E. Numerical calculation of the fluid dynamics of drop-on-demand jet. *IBM J. Res. Dev*. **1984**, *28*, 323–333, https://doi.org/10.1147/rd.283.0322.
15. Asai, A. Three-Dimensional Calculation of Bubble Growth and Drop Ejection in a Bubble Jet Printer. *J. Fluids Eng* **1992**, *114*, 638–641, https://doi.org/10.1115/1.2910079.
16. Liou, T.M.; Shih, K.C.; Chau, S.W.; Chen, S.C. Three-dimensional simulations of the droplet formation during the inkjet printing process. *Int. Comm. Heat Mass Transfer* **2002**, *29*, 1109–1118, https://doi.org/10.1016/S0735-1933(02)00439-6.
17. Roger, T. *Navier–Stokes Equations, Theory and Numerical Analysis.* AMS Chelsea**,** 2001; pp. 107–112.
18. Holdeman, J.T. A Hermite finite element method for incompressible fluid flow. *Int. J. Numer. Meth. Fluids* **2010**, *64*, 376–408, https://doi.org/10.1002/fld.2154.
19. Holdeman, J.T.; Kim, J.W. Computation of incompressible thermal flows using Hermite finite elements. *Comput. Meth. Appl. Mech. Eng.* **2010**, *199,* 3297–3304, https://doi.org/10.1016/j.cma.2010.06.036.
20. Potter, M.; Wiggert, D.C. *Schaum's Outlines, Fluid Mechanics, (Schaum's Series)*. McGraw-Hill (USA), 2008.
21. Nunes, P.S.; Ohlsson, P.D.; Ordeig, O.; Kutter, J.P. Cyclic olefin polymers: Emerging materials for lab-on-a-chip applications. *Microfluid. Nanofluid* **2010**, *9*, 145–161, https://doi.org/10.1007/s10404-010-0605-4.
22. Hirt, C.W.; Nichols, B.D. Volume of fluid (VOF) method for the dynamics of free boundaries. *J. Comput. Phys* **1981**, *39*, 201–225, https://doi.org/10.1016/0021-9991(81)90145-5.
23. Keller, S.; Blagoi, G.; Lillemose, M.; Haefliger, D.; Boisen, A. Processing of thin SU-8 films. *J. Micromech. Microeng.* **2008**, *18*, 125020.
24. Youngs, D.L. Time-Dependent Multi-material Flow with Large Fluid Distortion Fluid Dyn. *Academic Press* **1982**, 273–285.
25. Chemtob, A.; Ni, L.; Dietlin, C.; Croutxé-Barghorn, C.; Kitzmann, P.; Brogly, M.; Vidal, L. Spontaneous photoinduced formation of hybrid polymer films with functionalized macroporous patterns. *Surf. Coat. Technol.* **2012**, *209*, 64–72, https://doi.org/10.1016/j.surfcoat.2012.08.030.
26. Bousfield, D.W.; Keunings, R.; Marrucci, G.; Denn, M.M. Nonlinear Analysis of the Surface Tension Driven Breakup of Viscoelastic Filaments. *J. of Non-Newtonian Fluid mechanics* **1986**, *21*, 79–97, https://doi.org/10.1016/0377-0257(86)80064-7.
27. De Paz, H.; Chemtob, A.; Croutxé-Barghorn, C.; Le Nouen, D.; Rigolet, S. Insights into Photoinduced Sol-Gel Polymerization: An in Situ Infrared Spectroscopy Study. *J. Phys. Chem. B* **2012**, *116*, 5260–5268, https://doi.org/10.1021/jp212386e.
28. Baride, A.; Meruga, J.M.; Douma, C.; Langerman, D.; Crawford, G.; Kellar, J.J.; Cross, W.M.; May, P.S. A NIR-to-NIR upconversion luminescence system for security printing applications. *RSC Adv.* **2015**, *5*, 101338–101346, https://doi.org/10.1039/C5RA20785A.
29. Sears, F.W. Zemanski, M.W. *University Physics 2nd ed.* Addison Wesley, 1995.
30. Bao, B.; Li, M.; Li, Y.; Jiang, J.; Gu, Z.; Zhang, X.; Jiang, L.; Song, Y. Patterning fluorescent quantum dot nanocomposites by reactive inkjet printing. *Small* **2015**, *11*, 1649–1654, https://doi.org/10.1002/smll.201403005.
31. Wu, H.C.; Lin, H.J. Effects of Actuating Pressure Waveforms on the Droplet Behavior in a Piezoelectric Inkjet. *Materials Transactions* **2012**, *51*, 2269-2276, http://dx.doi.org/10.2320/matertrans.M2010123.
32. Lee, W.H.; Park, Y.D. Inkjet Etching of Polymers and Its Applications in Organic Electronic Devices. *Polymers* **2017**, *9*, 441, https://doi.org/10.3390/polym9090441.
33. Homola, T.; Shekargoftar, M.; Dzik, P.; Krumpolec, R.; Durasova, Z.; Vesely, M.; Cernak, M. Low-temperature (70 ◦C) ambient air plasma-fabrication of inkjet-printed mesoporous TiO2 flexible photoanodes. *Flex. Print. Electron.* **2017**, *2*, https://doi.org/10.1021/acsami.6b09556.
34. Sun, J.Z.; Guo, Y.Z.; Cui, B.; Chu, F.Q.; Li, H.Z.; Li, Y.; He, M.; Ding, D.; Liu, R.P.; Li, L.H.; Song, Y. Inkjet printing bendable circuits based on an oil-water interface reaction. *Appl. Surf. Sci.* **2018**, *445*, 391–397, https://doi.org/10.1016/j.apsusc.2018.03.204.
35. Sun, J.Z.; Yun, C.; Cui, B.; Li, P.; Liu, G.; Wang, X.; Chu, F. A Facile Approach for Fabricating Microstructured Surface Based on Etched Template by Inkjet Printing Technology. *Polymers* **2018**, *10*, 1209, https://dx.doi.org/10.3390%2Fpolym10111209.
36. Sun, J.Z.; Cui, B.; Chu, F.Q.; Yun, C.H.; He, M.; Li, L.H.; Song, Y.L. Printable nanomaterials for the fabrication of high-performance supercapacitors. *Nanomaterials* **2018**, *8*, 528, https://doi.org/10.3390/nano8070528.
37. Monajjemi, M.; Farahani,N.; Mollaamin,F.; Thermodynamic study of solvent effects on nanostructures: hosphatidylserine and phosphatidylinositol membranes. *Physics and Chemistry of Liquids* **2012**, *50*, 161-172, https://doi.org/10.1080/00319104.2010.527842.
38. Monajjemi, M.; Ahmadianarog, M.; Carbon Nanotube as a Deliver for Sulforaphane in Broccoli Vegetable in Point of Nuclear Magnetic Resonance and Natural Bond Orbital Specifications. *Journal of Computational and Theoretical Nanoscience* **2014**, *11,* 1465-1471, https://doi.org/10.1166/jctn.2014.3519.
39. Monajjemi, M.; Ghiasi, R.; Ketabi, S.; Passdar, H.; Mollaamin, F. A theoretical study of metal-stabilised rare tautomers stability: N4 metalated cytosine (M= Be2+, Mg2+, Ca2+, Sr2+ and Ba2+) in gas phase and different solvents, *Journal of Chemical Research* **2004**, *11,* https://doi.org/10.3184/030823404323000648.
40. Mollaamin, F.; Gharibe, S.; Monajjemi, M. Synthesis of various nano and micro ZnSe morphologies by using hydrothermal method. *International Journal of Physical Sciences* **2011**, *6*, 1496-1500.
41. Ardalan, T.; Ardalan, P.; Monajjemi, M. Nano theoretical study of a C 16 cluster as a novel material for vitamin C carrier. *Fullerenes Nanotubes and Carbon Nanostructures* **2014**, *22*, 687-708, https://doi.org/10.1080/1536383X.2012.717561.
42. Mahdavian, L.; Monajjemi, M.; Mangkorntong, N. Sensor response to alcohol and chemical mechanism of carbon nanotube gas sensors. *Fullerenes Nanotubes and Carbon Nanostructures* **2009,** *17*, 484-495, https://doi.org/10.1080/15363830903130044.
43. Monajjemi, M.; Najafpour, J. Charge density discrepancy between NBO and QTAIM in single-wall armchair carbon nanotubes. *Fullerenes Nanotubes and Carbon Nano structures* **2014,** *22*, 575-594, https://doi.org/10.1080/1536383X.2012.702161.
44. Monajjemi, M.; Hosseini, M.S. Non bonded interaction of B16 N16 nano ring with copper cations in point of crystal fields. *Journal of Computational and Theoretical Nanoscience* **2013**, *10*, 2473-2477, https://doi.org/10.1166/jctn.2013.3233.
45. Monajjemi, M.; Mahdavian, L.; Mollaamin, F. Characterization of nanocrystalline silicon germanium film and nanotube in adsorption gas by Monte Carlo and Langevin dynamic simulation. *Bulletin of the Chemical Society of Ethiopia* **2008**, *22,* 277-286, https://doi.org/10.4314/bcse.v22i2.61299.
46. Lee, V.S.; Nimmanpipug, P.; Mollaamin, F.; Thanasanvorakun, S.; Monajjemi, M. Investigation of single wall carbon nanotubes electrical properties and normal mode

analysis: Dielectric effects. *Russian Journal of Physical Chemistry A* **2009**, *83*, 2288-2296, https://doi.org/10.1134/S0036024409130184.
47. Mollaamin, F.; Najafpour, J.; Ghadami, S.; Akrami, M.S.; Monajjemi, M. The electromagnetic feature of B N H (x = 0, 4, 8, 12, 16, and 20) nano rings:Quantum theory of atoms in molecules/NMR approach. *Journal of Computational and Theoretical Nanoscience* **2014**, *11*, 1290-1298. https://doi.org/10.1166/jctn.2014.3495.
48. Monajjemi, M.; Mahdavian, L.; Mollaamin, F.; Honarparvar, B. Thermodynamic investigation of enolketo tautomerism for alcohol sensors based on carbon nanotubes as chemical sensors. *Fullerenes Nanotubes and Carbon Nanostructures* **2010**, *18*, 45-55, https://doi.org/10.1080/15363830903291564.
49. Monajjemi, M.; Ghiasi, R.; Seyed Sadjadi, M.A. Metalstabilized rare tautomers: N4 metalated cytosine (M = Li , Na, K , Rb and Cs), theoretical views. *Applied Organometallic Chemistry* **2003**, *17,* 635-640, https://doi.org/10.1002/aoc.469.
50. Ilkhani, A.R.; Monajjemi, M. The pseudo Jahn-Teller effect of puckering in pentatomic unsaturated rings C AE , A=N, P, As, E=H, F, Cl. *Computational and Theoretical Chemistry* **2015**, *1074*, 19-25, http://dx.doi.org/10.1016%2Fj.comptc.2015.10.006.
51. Monajjemi, M. Non-covalent attraction of B N and repulsion of B N in the B N ring: a quantum rotatory due to an external field. *Theoretical Chemistry Accounts* **2015,** *134*, 1-22, https://doi.org/10.1007/s00214-015-1668-9.
52. Monajjemi, M.; Naderi, F.;Mollaamin, F.; Khaleghian, M. Drug design outlook by calculation of second virial coefficient as a nano study. *Journal of the Mexican Chemical Society* **2012,** *56*, 207-211, https://doi.org/10.29356/jmcs.v56i2.323.
53. Monajjemi, M.; Bagheri, S.; Moosavi, M.S. Symmetry breaking of B2N(-,0,+): An aspect of the electric potential and atomic charges. *Molecules* **2015,** *20*, 21636-21657. https://doi.org/10.3390/molecules201219769.
54. Monajjemi, M.; Mohammadian,N.T. S-NICS: An aromaticity criterion for nano molecules. *Journal of Computational and Theoretical Nanoscience* **2015**, *12*, 4895-4914, https://doi.org/10.1166/jctn.2015.4458.
55. Monajjemi, M.; Ketabi, S.; Hashemian Zadeh, M.; Amiri, A. Simulation of DNA bases in water: Comparison of the Monte Carlo algorithm with molecular mechanics force fields. *Biochemistry (Moscow)* **2006**, *71 (SUPPL. 1),* S1-S8, https://doi.org/10.1134/s0006297906130013.
56. Monajjemi, M.; Lee, V.S.; Khaleghian, M.; Honarparvar, B.; Mollaamin, F. Theoretical Description of Electromagnetic Nonbonded Interactions of Radical, Cationic, and Anionic NH2BHNBHNH2 Inside of the B18N18 Nanoring. *J. Phys. Chem C* **2010**, *114*, 15315, https://doi.org/10.1021/jp104274z.
57. Monajjemi, M.; Boggs, J.E. A New Generation of BnNn Rings as a Supplement to Boron Nitride Tubes and Cages. *J. Phys. Chem. A* **2013**, *117*, 1670-1684, http://dx.doi.org/10.1021/jp312073q.
58. Monajjemi, M. Non bonded interaction between BnNn (stator) and BN B (rotor) systems: A quantum rotation in IR region. *Chemical Physics* **2013**, *425*, 29-45, https://doi.org/10.1016/j.chemphys.2013.07.014.
59. Monajjemi, M.; Robert, W.J.; Boggs, J.E. NMR contour maps as a new parameter of carboxyl's OH groups in amino acids recognition: A reason of tRNA–amino acid conjugation. *Chemical Physics* **2014**, *433*, 1-11, https://doi.org/10.1016/j.chemphys.2014.01.017.
60. Monajjemi, M. Quantum investigation of non-bonded interaction between the B15N15 ring and BH2NBH2 (radical, cation, and anion) systems: a nano molecularmotor. *Struct Chem* **2012,** *23*, 551–580, http://dx.doi.org/10.1007/s11224-011-9895-8.
61. Monajjemi, M. Metal-doped graphene layers composed with boron nitride–graphene as an insulator: a nano-capacitor. *Journal of Molecular Modeling* **2014**, *20*, 2507, https://doi.org/10.1007/s00894-014-2507-y.
62. Monajjemi M. Graphene/(h-BN)*n*/X-doped raphene as anode material in lithium ion batteries (X = Li, Be, B AND N). *Macedonian Journal of Chemistry and Chemical Engineering* **2017**, *36*, 101–118, http://dx.doi.org/10.20450/mjcce.2017.1134.
63. Monajjemi, M. Cell membrane causes the lipid bilayers to behave as variable capacitors: A resonance with self-induction of helical proteins. *Biophysical Chemistry* **2015**, *207*, 114-127, https://doi.org/10.1016/j.bpc.2015.10.003.
64. Monajjemi, M. Study of CD5+ Ions and Deuterated Variants (CHxD(5-x)+): An Artefactual Rotation. *Russian Journal of Physical Chemistry a* **2018,** *92*, 2215-2226. https://doi.org/10.1134/S0036024418110286.
65. Monajjemi, M. Liquid-phase exfoliation (LPE) of graphite towards graphene: An ab initio study. *Journal of Molecular Liquids* **2017**, *230*, 461–472, https://doi.org/10.1016/j.molliq.2017.01.044.
66. Jalilian, H.; Monajjemi, M. Capacitor simulation including of X-doped graphene (X = Li, Be, B) as two electrodes and (hBN)m (m = 1–4) as the insulator. *Japanese Journal of Applied Physics* **2015**, *54,* 085101-7.

6. ACKNOWLEDGEMENTS

The authors would like to appreciate Ministry of Science and Technology of Vietnam for funding this research under the grant number 03/2019/HĐ-SPĐP.